Climate Dynamics (2022) 59:245–261
https://doi.org/10.1007/s00382-021-06124-w

Oceanic meridional transports and their roles in warm water volume variability and ENSO in the tropical Pacific

Xiaofan Li[1,2,3] · Zeng-Zhen Hu[4] · Bohua Huang[5] · Fei-Fei Jin[6]

Received: 16 July 2021 / Accepted: 28 December 2021 / Published online: 9 January 2022

Abstract
The fluctuation of the subsurface ocean heat condition along the equatorial Pacific is associated with the mass/heat exchanges between the equatorial and off-equatorial regions, which is the main cause of the phase transitions during the El Niño–Southern Oscillation (ENSO) cycle. In this work, the connection between the meridional transport convergences (MTCs) along the equatorial Pacific and variations of the warm water volume in the equatorial Pacific and their connections with the ENSO cycle are investigated. It is noted that the Sverdrup MTC induced by the wind stress curl has a significant impact on the thermocline fluctuation in nearly the entire equatorial Pacific but the impacts of its components vary with longitude. The component induced by the Ekman currents has a significant contribution from 150° W eastward to the coast, as well as the far-western Pacific, while the geostrophic component has a significant contribution in the central Pacific. There is a strong compensation between the surface wind stress-induced Ekman MTC and the Ekman pumping-induced geostrophic MTC which is confined in the central Pacific. Furthermore, the geostrophic component facilitates the phase transition of the ENSO cycle, while the Ekman component compensatively hinders it. The longitudinally varying component of the MTC enhances the anomalous thermocline tilting during the ENSO growth and maturing phases. These results may benefit the understanding, monitoring, and forecasting of ENSO evolution.

1 Introduction

Climate anomalies may cause serious social crises and affect economic growth. Accurately predicting climate variability has great social and economic benefits (National Research Council 2010). At interseasonal-to-interannual time scales, the predictability of global climate variability is linked to the tropical forcing that is mainly associated with the El Niño–Southern Oscillation (ENSO) (National Research Council 2010; Wang et al. 2016; Huang et al. 2019; Hu et al. 2020a, b). Thus, understanding and predicting ENSO evolution are crucial for global interseasonal-to-interannual climate prediction.

As a coupled irregular oscillation in the tropical Pacific, ENSO growth is linked to the positive feedbacks among the oceanic thermocline fluctuation, atmospheric deep convection, sea surface temperature (SST), and surface wind stress anomalies in the central and eastern equatorial Pacific (Bjerknes 1969). Meanwhile, the interaction between the equatorial and off-equatorial oceans generates the heat discharge/recharge of the equatorial zone, which modulates the ENSO recurrence and leads to the phase transition of the ENSO cycle. Wyrtki (1985) first pointed out that subsurface oceanic condition is crucial for El Niño evolution, and the period/cycle of ENSO is determined by the rate of accumulation and dispersion of the ocean heat in the equatorial Pacific. Later, through theoretical modeling, Jin (1997a, b) documented that the recharge–discharge of the equatorial Pacific heat content generates the non-equilibrium

✉ Xiaofan Li
xiaofanli@zju.edu.cn

1 Key Laboratory of Geoscience Big Data and Deep Resource of Zhejiang Province, School of Earth Sciences, Zhejiang University, Hangzhou 310027, Zhejiang, China

2 Southern Marine Science and Engineering Guangdong Laboratory (Zhuhai), Zhuhai 519082, China

3 Department of Atmospheric Sciences, School of Earth Sciences, Zhejiang University, Zhejiang, China

4 Climate Prediction Center, NCEP/NWS/NOAA, College Park, MD 20740, USA

5 Department of Atmospheric, Oceanic, and Earth Sciences, College of Science, George Mason University, Fairfax, VA 22030, USA

6 Department of Atmospheric Sciences, University of Hawaii at Manoa, Honolulu, HI 96822, USA

between the zonal-mean equatorial thermocline depth and wind stress: an El Niño (a La Niña) event depletes (resupplies) the equatorial heat content and leads to a shallower (deeper) mean thermocline in the equatorial Pacific. The heat accumulation and depletion in the equatorial Pacific Ocean determine the phase transition and amplitude of the ENSO cycle (Zebiak 1989) that leads to the cyclic evolution of ENSO (Kessler 2002).

The fluctuation of ocean subsurface heat is reflected in the equatorial warm water volume (WWV) mode (Clarke et al. 2007; Clarke 2010; Kumar and Hu 2014; Hu et al. 2017a), which can be measured by the WWV index as the anomalous volume of water above the 20 °C isotherm (D20) in the entire equatorial Pacific (e.g., Meinen and McPhaden 2000; Brown and Fedorov 2010). The WWV tends to be highest (lowest) during the developing stage of an El Niño (La Niña) event. Geographically, the subsurface oceanic heat buildup and reduction are concentrated in the western and central Pacific (Li et al. 2020) and are associated with the strengthening and relaxation of the trade winds. While the equatorial easterly trade winds weaken (strengthen), the positive (negative) thermocline anomaly in the western equatorial Pacific propagates eastward in the form of a Kelvin wave. That leads to a reduction (an enhancement) of the thermocline slope and initiates an El Niño (a La Niña) event (Wyrtki 1975; Clarke 2010). As the accumulated ocean heat content redistributes zonally throughout the basin, it is also discharged into higher latitudes as the El Niño peaks and decays. Conversely, ocean heat content is recharged into the equatorial ocean as the La Niña peaks and decays (Jin 1997a, b). Such heat exchanging between the equatorial and off-equatorial oceans is mainly accomplished through Sverdrup transports across the latitudinal circles of the equator, which is induced by the off-equatorial wind stress curls on both sides of the equator (Jin 1997a). Thus, the variations of the equatorial upper-ocean heat content are controlled by the interplay among meridional, zonal, and vertical transports (Brown and Fedorov 2010).

The variation of WWV, the accumulated heat content in the equatorial Pacific, is considered to be a crucial precursor for ENSO forecast and is also the major source of the ENSO predictability (e.g., Clarke and Van Gorder 2001; Kug et al. 2005; McPhaden et al. 2006; McGregor et al. 2014; Tseng et al. 2016; Huang et al. 2017; Clarke and Zhang 2019; Hu et al. 2019, 2020b; Chen et al. 2020). Observationally, the variation of the WWV mode leads the ENSO evolution by a couple of seasons (e.g., Wyrtki 1975, 1985; Meinen and McPhaden 2000; McPhaden 2012; Singh and Delcroix 2013; Hu et al. 2017b; Izumo et al. 2019; Zhang et al. 2019; Li et al. 2020; Zhao et al. 2021). Since WWV is determined by heat exchange between the equatorial and off-equatorial ocean, which is dominated by meridional mass transport convergence (MTC), to better understand and forecast the ENSO cycle requires a thorough examination of the contributions by the various meridional transport processes to the variation of WWV in connection with the ENSO cycle.

Previous studies have concentrated on the roles played by the meridional water and heat exchanges between the equatorial and off-equatorial Pacific on driving the time tendency of WWV. On the other hand, the zonal pressure gradient along the equator associated with the slope of the anomalous thermocline depth is largely in a Sverdrup balance with the equatorial wind stress force (e.g., Cane and Sarachik 1981; McPhaden and Taft 1988; Schneider et al. 1995; Yu and McPhaden 1999). This quasi-equilibrium is used to explain the zonal tilt mode of the equatorial thermocline during the ENSO peak phases (e.g., Meinen and McPhaden 2001). In the discharge/recharge paradigm, the Sverdrup balance is assumed to hold all the time (Jin 1997a, b; Clarke et al. 2007). Chen et al. (2016) pointed out that the Sverdrup balance may not hold during the ENSO peaking phases when a sudden reversal of the anomalous zonal water transport occurs in the eastern equatorial Pacific, which triggers a quick decay of the ENSO events. More recently, Zhang and Clarke (2017) and Clarke and Zhang (2019) showed that the anomalous zonal flow acceleration right at the equator is crucial to understanding the WWV-El Niño dynamics. Therefore, it is useful to explore that, in addition to equatorial zonal winds, what other factors can affect the zonal pressure gradient (i.e., the tilt mode) along the equator.

Using reanalysis data in this work, we investigate the contribution of the convergence of the Sverdrup transport along the equatorial Pacific to the variations of thermocline fluctuation of the equatorial Pacific and WWV. In particular, we focus on the longitudinal dependence of the contributions and their lead–lag connection with ENSO. We further decompose the Sverdrup transport into its Ekman and geostrophic components and examine their contributions to the thermocline fluctuations along the equator. The characteristics of the MTCs and their longitudinal variations along the equatorial Pacific are examined in connection with the variations of the equatorial thermocline, as well as the integral properties, such as the WWV and ENSO indices. These features, especially their longitudinal dependence and association with the ENSO cycle, have not been fully examined in previous work. The paper is organized as follows. The data and methods used in the analysis are described in Sect. 2; Sects. 3 and 4 present the integral properties and longitudinal variations of the MTCs, respectively; Sect. 5 shows the connection of the MTCs with the ENSO cycle; a summary with discussion is given in Sect. 6.

2 Data and methods

The fluctuation of the equatorial Pacific thermocline is measured by the gridded monthly mean D20 from the Global Ocean Data Assimilation System with a resolution of 1° latitude by

1° longitude (GODAS; Behringer 2007). The recharge and discharge processes (Wyrtki 1975, 1985; Jin 1997a, b; Wang 2001) are represented by the WWV index, which is defined as the monthly mean D20 anomaly (D20a) averaged over the region within 5° S–5° N, 120° E–80° W (Meinen and McPhaden 2000). ENSO is measured using the Niño3.4 index defined as the monthly mean SST anomaly (SSTA) averaged over the region within 5° S–5° N, 120° W–170° W. The SST is represented by the monthly mean ocean temperature of the top layer (5 m) of GODAS. The monthly mean ocean surface wind stress is from the National Environmental Prediction Center and Department of Energy reanalysis (Kanamitsu et al. 2002). The data duration is January 1979–December 2019. The monthly mean anomalies are calculated relative to the climatologies in the entire period.

According to Clarke et al. (2007) and Bosc and Delcroix (2008), the wind-driven variations of ocean thermocline depth at different longitudes along the equator, which are represented by the time tendency of the averaged D20a from 5° S to 5° N, can be approximated as:

$$\frac{\partial \mathrm{D20a}}{\partial t} = \frac{V_S - V_N}{L_y} + \frac{T_W - T_E}{L_x} \tag{1}$$

where L_y is the distance from 5° S to 5° N and L_x is the length of one longitudinal grid on the equator; V_S and V_N are the anomalous meridional volume transports (vertically integrated meridional velocity) above D20 at 5° S and 5° N; T_W and T_E are the anomalous zonal transports at the west and east sides of a longitudinal grid along the equator, respectively. With the assumption of the seawater density as constant, the volume transport and mass transport variations are equivalent, except for the unit and magnitude differences. In the following discussion, we concentrate on the meridional transports V_S and V_N and simply refer them as the transports unless otherwise noted. For convenience, T_{120E} and T_{80W} are referred specifically to as the zonal transports from the western and eastern boundaries of the considered domain at 120° E and 80° W, respectively, hereafter.

In this study, we calculate V_S and V_N (the total MTC) from GODAS as the meridional current anomalies integrated from D20 to the ocean surface. We will demonstrate that a considerable portion of V_S and V_N is caused by the Sverdrup transport, which is the part of the meridional transport driven by surface wind stress curl as:

$$V_{Sv} = \frac{1}{\rho\beta}\left(\frac{\partial \tau_y}{\partial x} - \frac{\partial \tau_x}{\partial y}\right) \tag{2}$$

where ρ is seawater density; $\beta = \frac{df}{dy}$, and $f = 2\Omega\sin\varphi$ is the Coriolis parameter; Ω is the angular speed of the earth's rotation; φ is the latitude; τ_x and τ_y are zonal and meridional wind stress anomalies, respectively. The unit of the transport is m^2/s.

The Sverdrup transport (V_{Sv}) can be further decomposed into two types of transports: the geostrophic (V_{ge}) and Ekman (V_{Ek}) transport, i.e.

$$V_{Sv} = V_{ge} + V_{Ek} \tag{3}$$

The geostrophic current is a balanced flow between the Coriolis force and the pressure gradient force throughout the layer of the upper ocean, while the Ekman current is a direct response to the surface wind stress forcing in the planetary boundary layer (roughly the oceanic mixed layer) under the combined influences of the Coriolis force and turbulent mixing. Following Pedlosky (1996), the Ekman (V_{Ek}) and geostrophic (V_{ge}) transports at latitude φ are

$$V_{Ek} = -\frac{1}{\rho f}\tau_x \tag{4}$$

$$w_{Ek} = \frac{1}{\rho}\left[\frac{\partial}{\partial x}\left(\frac{\tau_y}{f}\right) - \frac{\partial}{\partial y}\left(\frac{\tau_x}{f}\right)\right] \tag{5}$$

$$V_{ge} = \frac{f}{\beta} w_{Ek} = R\tan\varphi w_{Ek} \tag{6}$$

where R is the radius of the earth; w_{Ek} is the Ekman vertical velocity (upwelling or downwelling at the bottom of the oceanic mixed layer). Therefore, the meridional geostrophic transport is a response to the vortex stretching by the Ekman pumping.

It should be indicated that the results from Eqs. (1 to 6) are varied with longitude. Here, in addition to discussing the longitudinal variations of 5° S–5° N average or convergence, we also examine their zonal averages of 120° E–80° W. $\frac{\partial \mathrm{D20a}}{\partial t}$ averaged in 120° E–80° W is used to represent $\frac{\mathrm{dWWV}}{\mathrm{dt}}$.

3 Basin integral properties

Climatologically, the MTC between 5° S and 5° N in the Pacific is negative for the Ekman component (Fig. 1d) because the easterly winds prevailing over the tropical Pacific generate poleward Ekman transport at both 5° N and 5° S. The geostrophic component is convergent (Fig. 1e) due to the off-equatorial downwelling on both sides of the equator. Both are with maximum values in the central-eastern Pacific. The Sverdrup MTC between 5° S and 5° N is the compensated result between the two components and is negative (positive) in the 1st (2nd) half of the year (Fig. 1c). To some extent, the seasonal cycle of the Sverdrup MTC is similar to that of the total MTC (Fig. 1b) and the climatological monthly tendency of the

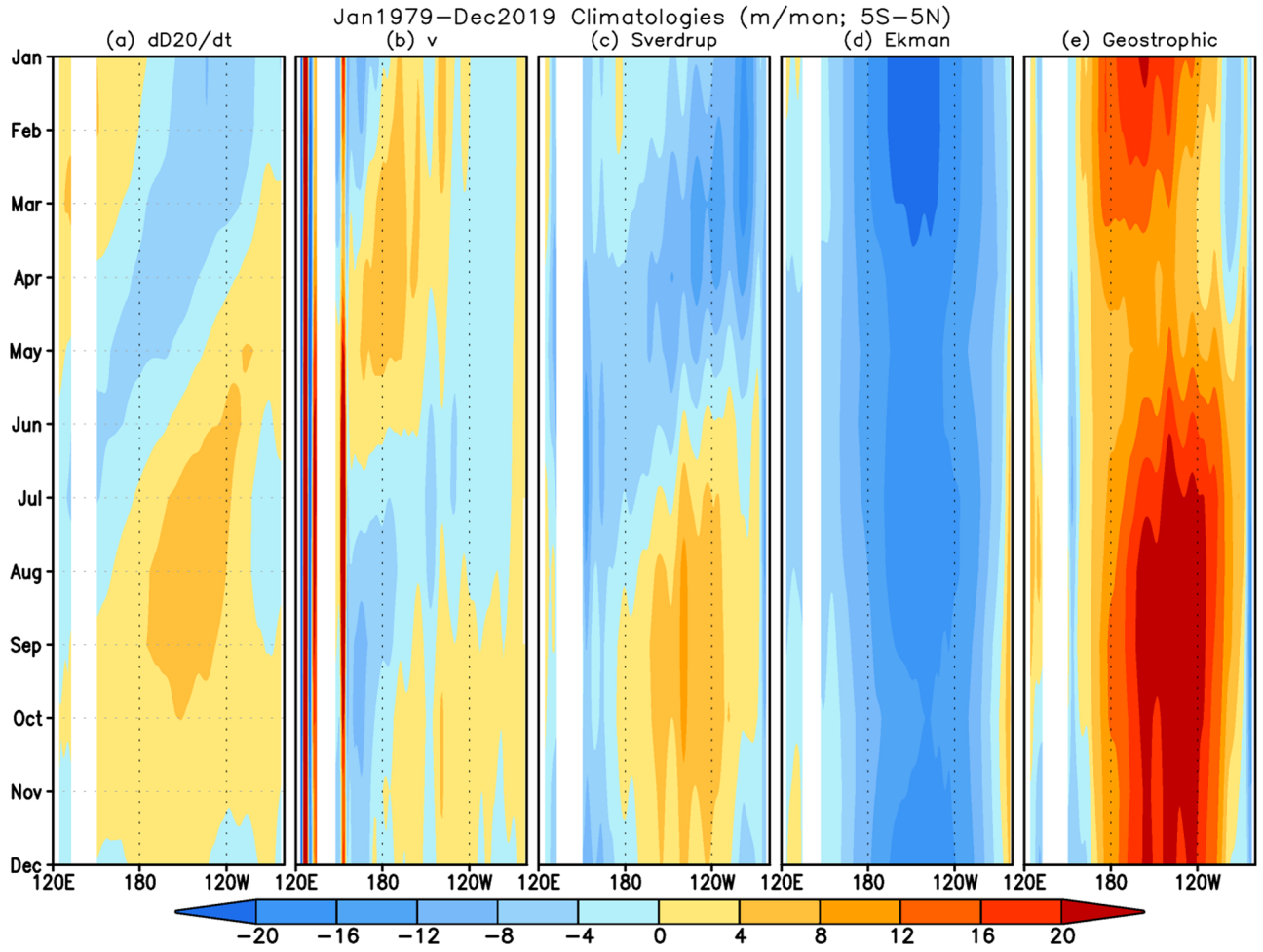

Fig. 1 Seasonal cycle of **a** the climatological monthly tendency of the thermocline (D20) averaged in 5° S–5° N and the convergences of the **b** total meridional transport integrated from the thermocline (D20) to the oceanic surface, **c** Sverdrup, **d** Ekman, and **e** geostrophic meridional transport convergence between 5° S and 5° N averaged in January 1979–December 2019. The unit is m/month

thermocline (Fig. 1a), which show pronounced westward propagation.

Before studying the longitudinal and anomalous variations, we first examine the integral properties of the upper-ocean heat content anomalies. It is noted that the time evolution of the Sverdrup MTC between 5° S and 5° N averaged in 120° E–80° W well represents the time tendency of WWV anomaly (i.e., $\frac{dWWV}{dt}$) with a significant simultaneous correlation of 0.48 as well as the total MTC with a significant simultaneous correlation of 0.51 (Fig. 2a). For a direct and quantitative comparison, both the tendencies of WWV and D20a ($\frac{dWWV}{dt}$, $\frac{\partial D20a}{\partial t}$) and all the MTCs are displayed in the unit of m/month in this work. The coherence between $\frac{dWWV}{dt}$ and the total and Sverdrup MTCs is evident especially during the major El Niño and La Niña episodes. Nevertheless, only about 25% of the variances of $\frac{dWWV}{dt}$ and the total MTC can be explained by the Sverdrup MTC, meaning that other processes may play important roles in offsetting the contribution from the Sverdrup MTC to $\frac{dWWV}{dt}$.

One possibility of the overly strong Sverdrup MTC is that the wind-driven transports may extend below the level of D20. Since D20 is not exactly a material surface, vertical mass and heat transports across the 20 °C surface may also play an important role in ENSO evolution (e.g., Meinen and McPhaden 2001; Clarke et al. 2007; Bosc and Delcroix 2008). On the other hand, Lengaigne et al. (2021) emphasized the importance of equatorial diabatic processes in controlling WWV variations. Also, as a reanalysis system, GODAS does not conserve mass or energy because of assimilating data, which may add additional biases to the budget calculations here.

Moreover, the zonal transports through the western (e.g., Indonesian through flow) and eastern boundaries of the domain (T_{120E} and T_{80W}) have some contributions to $\frac{dWWV}{dt}$ (Fig. 3) although they have much smaller amplitudes

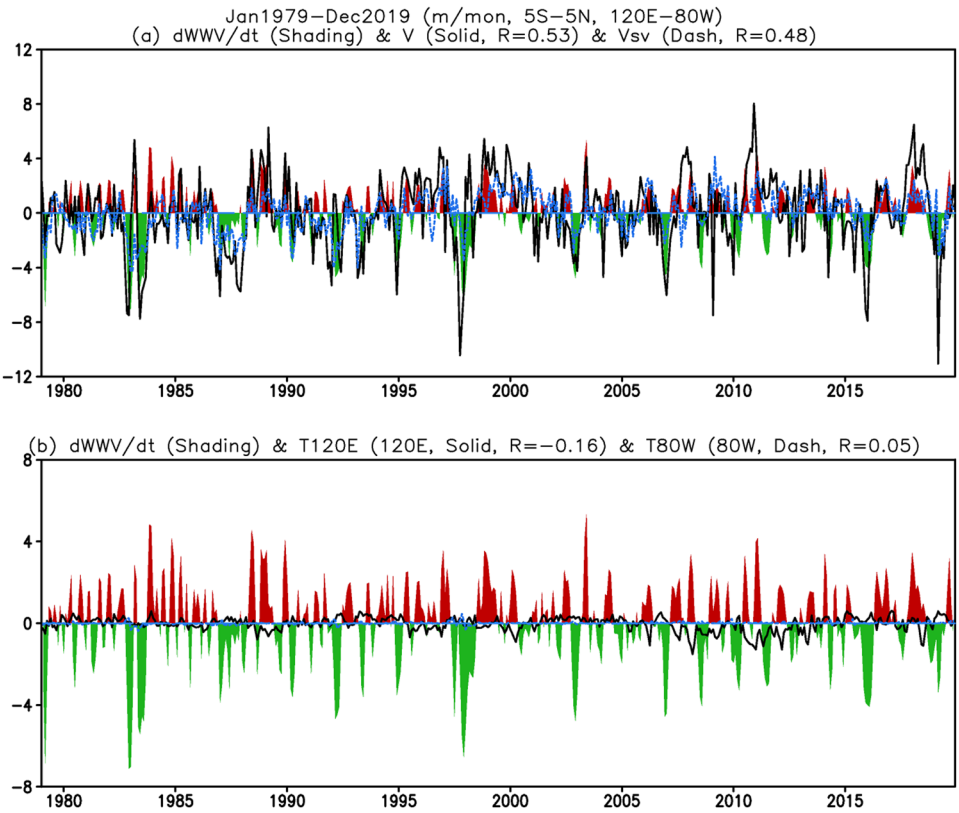

Fig. 2 Time series of $\frac{dWWV}{dt}$ (shading, **a**, **b**), the total (black solid line, a) and Sverdrup (blue dashed line, **a**) MTC between 5° S and 5° N and averaged in 120° E–80° W, T_{120E} (black solid line, **b**), and T_{80W} (blue dashed line, **b**). T_{120E} (T_{80W}) is referred to the contribution of the zonal current between 5° S and 5° N integrated from the thermocline (D20) to the oceanic surface across 120° E (80° W). The unit is m/month

and weaker correlations with $\frac{dWWV}{dt}$ (Fig. 2b) compared with that of the MTC terms (Fig. 2a). Here, the contributions of the zonal transport across the western (T_{120E}) (eastern (T_{E80W})) boundary to $\frac{dWWV}{dt}$ are defined as the anomalous zonal current averaged between 5° S and 5° N integrated from the thermocline (D20) to the oceanic surface across 120° E (80° W). The standard deviation of T_{120E} (0.35 m/mon) is larger than that of T_{80W} (0.06 m/mon). Nevertheless, they are much smaller than that of $\frac{dWWV}{dt}$ (2.0 m/mon), the geostrophic (3.2 m/mon), Ekman (2.1 m/mon), and Sverdrup (2.6 m/mon) MTCs. T_{120E} has significant negative contemporary correlations with $\frac{dWWV}{dt}$, the geostrophic and Sverdrup MTCs, while it has significant positive contemporary correlations with the Ekman MTC. On the contrary, the corresponding correlations with T_{80W} are not significant. That is generally consistent with Zebiak (1989), Springer et al. (1990), Lengaigne et al. (2021), and Lu et al. (2017). They emphasized that interior transports are partially compensated by the western boundary current transports. Lu et al. (2017) suggested that the zonal transport from the western boundary is highly correlated with meridional convergence and leads by about 4–5 months, and their phase offset determines the WWV variations.

Though with all these caveats, Fig. 2 shows that (1) the basin-averaged MTC above D20 is a major contributor to $\frac{dWWV}{dt}$, and (2) the basin-averaged Sverdrup MTC is a reasonably good approximation to the total interior ocean MTC. For the entire equatorial Pacific average (5° S–5° N, 120° E–80° W), the contemporary correlations of $\frac{dWWV}{dt}$ with the Sverdrup, geostrophic, and Ekman MTCs are 0.48, 0.24, and 0.22 (Table 1), respectively. Through linear regression and variance calculations, it is noted that about 23%, 5%, and 6% of the variance of $\frac{dWWV}{dt}$ can be explained simultaneously by the Sverdrup, geostrophic, and Ekman MTCs, respectively. The Sverdrup MTC has a positive correlation of 0.74 with the geostrophic component, and an insignificant correlation of 0.12 with the Ekman component (Table 1). The geostrophic component has a significant negative correlation of − 0.57 with the Ekman component (Table 1), suggesting a compensation between the two components, similar to the climatology (Fig. 1). Even though the correlations are statistically significant, they are still relatively small. Thus, it would be interesting to further examine the longitudinal variations.

4 Longitudinal variations

We further examine the longitudinal variations of the connections between $\frac{dD20a}{dt}$ and the MTCs. Figure 4 shows the time-longitude cross-sections of (a) $\frac{\partial D20a}{\partial t}$ averaged between

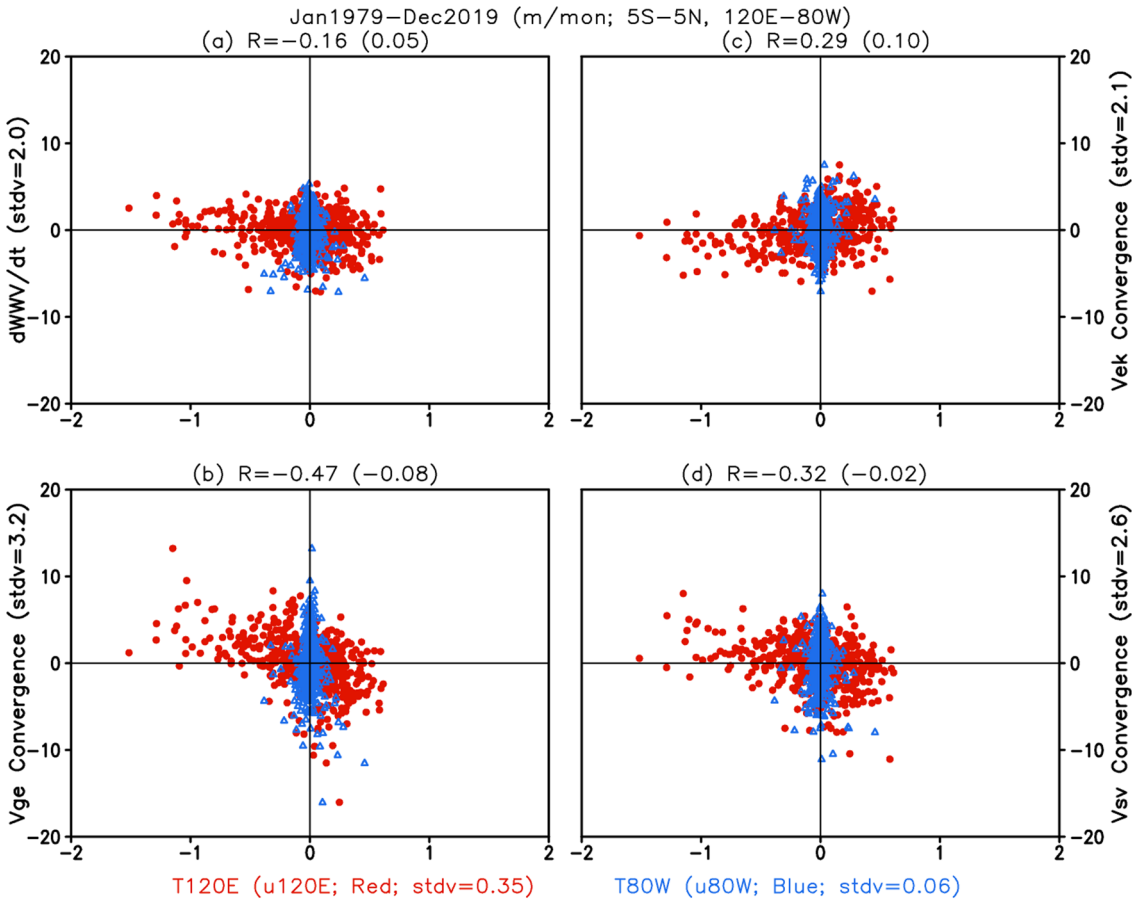

Fig. 3 Scatter plots of T_{120E} (red dots) and T_{80W} (blue triangles) with **a** $\frac{dWWV}{dt}$, **b** geostrophic, **c** Ekman, and **d** Sverdrup MTCs. The correlations with T_{120E} (T_{80W}) are shown in the subtitle of each panel (in the brackets). The stdv values represent the standard deviations

Table 1 Linear correlations among $\frac{dWWV}{dt}$, the Sverdrup (Vsv), geostrophic (Vge), and Ekman (Vek) MTCs in January 1979–December 2019; $\frac{dWWV}{dt}$ is $\frac{\partial D20a}{\partial t}$ averaged in 5° S–5° N, 120° E–80° W, and the MTCs are the differences between 5° S and 5° N and averaged in 120° E–80° W

	Vsv	Vge	Vek
$\frac{dWWV}{dt}$	0.48*	0.24*	0.22*
Vsv		0.74*	0.12
Vge			−0.57*

The correlation values with "*" mean significant at the 1% significance level using a t-test with independent sample sizes which are estimated following Bretherton et al. (1999)

5° S and 5° N, and the anomalous convergences of the (b) total meridional transports integrated from the thermocline to the oceanic surface, (c) Sverdrup, (d) Ekman, and (e) geostrophic MTCs between 5° S and 5° N. As in the integral cases, both the total MTC (Fig. 4b) and Sverdrup STC (Fig. 4c) show larger amplitudes than that of $\frac{\partial D20a}{\partial t}$ (Fig. 4a). The differences between Fig. 4a and b, c may also be associated with some processes that redistribute heat content zonally across the basin, such as the zonal wave propagation and the fluctuation of the tilting mode associated with the time variations of the equatorial zonal wind anomalies, which are not represented here. That may imply a limited role of MTCs in explaining the longitudinal-time fluctuations of $\frac{\partial D20a}{\partial t}$, especially for the variabilities in the higher frequencies. On the other hand, certain coherence is present between $\frac{\partial D20a}{\partial t}$ (Fig. 4a) and the total MTC (Fig. 4b) in the western and central equatorial Pacific, and between the Sverdrup (Fig. 4c) and total (Fig. 4b) MTCs at interseasonal and interannual time scales. Interestingly, the negative $\frac{\partial D20a}{\partial t}$ across the basin during the mature and decay phases of the strong El Niño events (e.g., 1983, 1998, 2007, and 2016, Fig. 4a) corresponds more closely with the Sverdrup MTC (Fig. 4c) than with those of the total MTC (Fig. 4b), especially in the eastern equatorial Pacific.

From Fig. 4d, e, we can see that there is a clear compensation between the geostrophic and Ekman transports, as noted in Izumo (2005) and Bosc and Delcroix (2008). Physically, the geostrophic and Ekman transports are interconnected to a certain degree. In the Northern (Southern) Hemisphere, the Ekman transport pushes

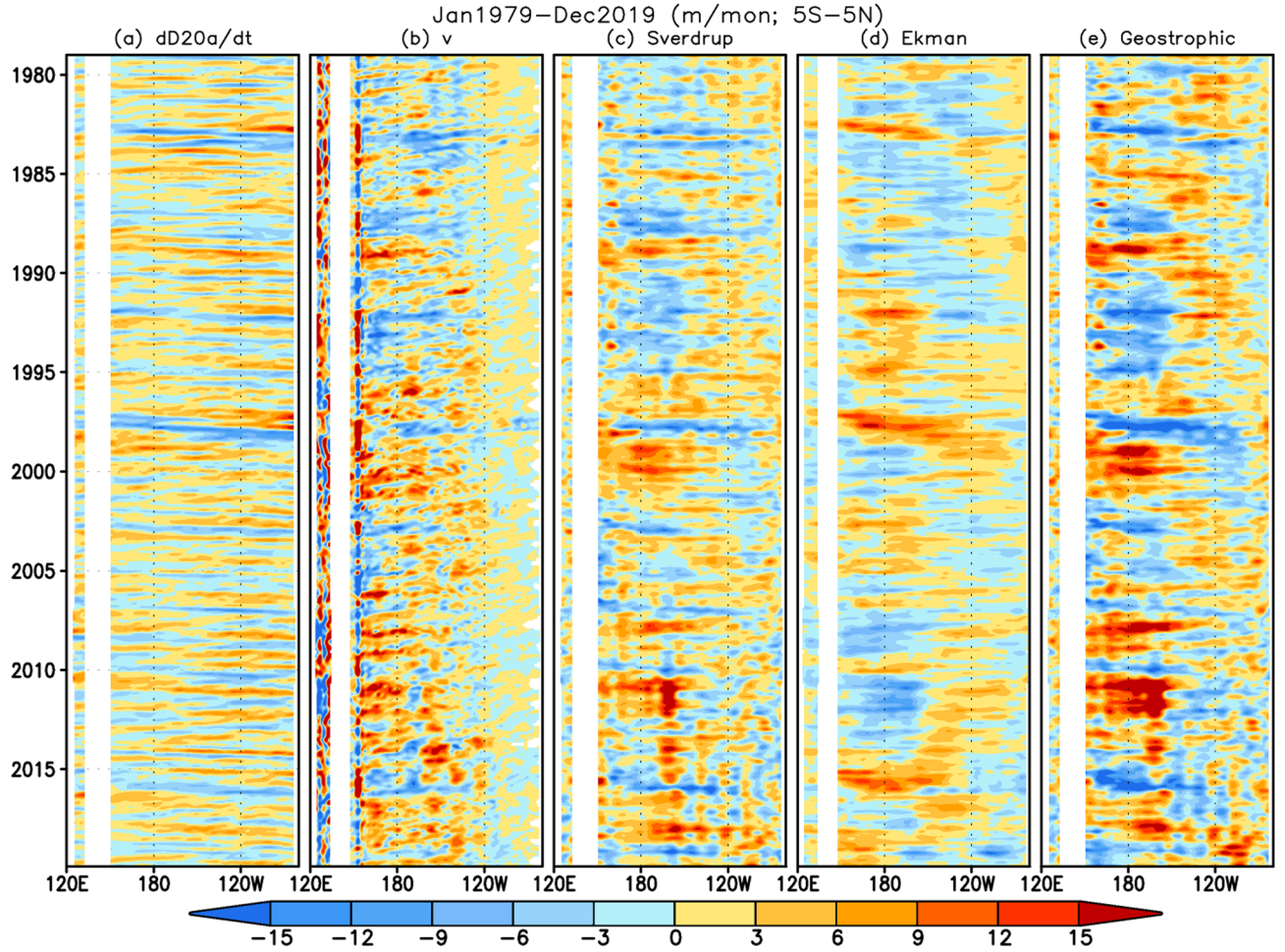

Fig. 4 Hovmöller diagrams of **a** $\frac{\partial D20a}{\partial t}$ averaged in 5° S–5° N and the anomalous convergences of the **b** total meridional transport integrated from the thermocline (D20) to the oceanic surface, **c** Sverdrup, **d** Ekman, and **e** geostrophic meridional transports between 5° S and 5° N. The unit is m/month

water to the right (left) of the direction of the surface wind stress, which creates a hill of seawater to one side of the prevailing winds. For instance, a westerly wind anomaly over the equatorial ocean with a meridional width of 20° latitudes causes equatorward Ekman transports from both hemispheres and volume convergence into the equatorial ocean. Furthermore, a jet-like structure of the westerly wind anomaly with the largest amplitude along the equator leads to a latitudinal variation of the Ekman transports: the transports decrease with latitude increase. Such latitudinal variation of the Ekman transport causes off-equatorial Ekman divergences and upwelling at the bottom of the mixed layer on both sides of the equator. These vertical movements tilt up the isopycnal below the mixed layer and cause poleward geostrophic currents. In this case, the Ekman and geostrophic transports tend to compensate each other.

In addition to the out-of-phase relation, the geostrophic MTC (Fig. 4e) generally has a larger amplitude than that of the Ekman MTC (Fig. 4d), as pointed out by Kug et al. (2003). Consistently, the geostrophic MTC (Fig. 4e) also has a larger amplitude than that of the Sverdrup MTC (Fig. 4c). This is confirmed by the longitudinal distributions of the standard deviations shown in Fig. 5a. The variability (measured by standard deviation) of the Sverdrup MTC (green curve, Fig. 5a) is smaller than that of the geostrophic component (black curve, Fig. 5a) and larger than that of the Ekman component (red curve, Fig. 5a). For the longitudinal variations, the standard deviations of all three MTCs are generally larger in the western and central Pacific (150° E–150° W) than in the eastern Pacific, which is similar to the longitudinal variation pattern of the standard deviation of the zonal wind stress anomaly (bar in Fig. 5b). A clear peak of standard deviation appears in the central Pacific around

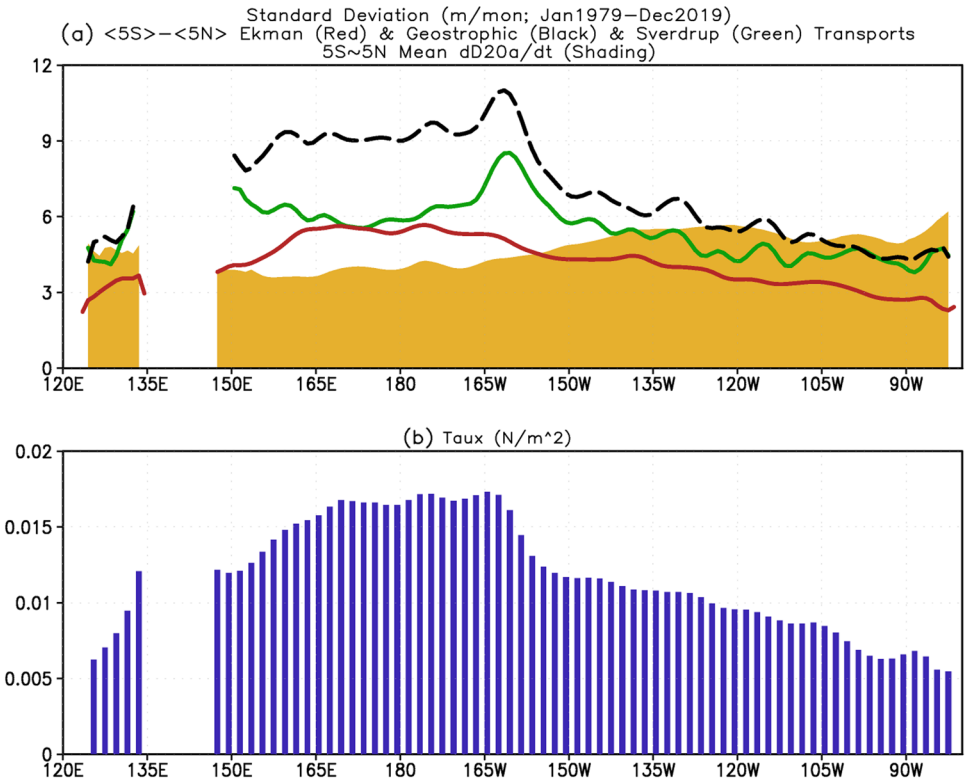

Fig. 5 Longitudinal evolution of standard deviations of **a** $\frac{\partial D20a}{\partial t}$ averaged in 5° S–5° N (shading) and the Ekman (red), geostrophic (black), and Sverdrup (green) MTCs between 5° S and 5° N, **b** zonal wind stress anomaly averaged in 5° S–5° N. The units are N/m^2 for the wind stress and m/month for the others

160°–165° W for both the geostrophic and Sverdrup MTCs, especially the latter, before being quickly reduced further east (Fig. 5a). A possible explanation is that this is near the nodal point where the MTCs change sign. Compared with the MTCs, the longitudinal variation of the standard deviation of $\frac{\partial D20a}{\partial t}$ is less obvious but is generally smaller in the west than in the east. The amplitude of $\frac{\partial D20a}{\partial t}$ (shading, Fig. 5a) is smaller than that of the MTCs in 155°E-155°W but is closer to the MTCs further east.

For the average between 5° S and 5° N, the MTCs are moderately correlated with $\frac{\partial D20a}{\partial t}$ on a broad zone along the equator, with the maximum correlation around 0.3–0.4. The contributions of the Ekman (red), geostrophic (black), and Sverdrup (green) MTCs to $\frac{\partial D20a}{\partial t}$ are different and vary with longitude (Fig. 6a). For the Ekman component (red curve, Fig. 6a), significant positive correlations appear from 150° W eastward to the coast as well as in the far-western Pacific, while the correlations are generally negative and not significant in the central Pacific (145° E–155° W). On the other hand, for the geostrophic component (black curve, Fig. 6a), significant positive correlations are present from the central to east-central Pacific (165° E–135° W) with some significant negative correlations in the far-western Pacific. In the eastern Pacific, the correlations are also negative but smaller.

For the Sverdrup MTC (green curve, Fig. 6a), significant positive correlations are present in almost the entire equatorial Pacific, except in the far-western and far-eastern Pacific. On its relations among the MTC components, the geostrophic and the Sverdrup MTC show high positive correlations in the whole longitude range (black curve, Fig. 6b). However, the significant correlation of the Ekman component with the Sverdrup MTC is confined in the central Pacific (green curve, Fig. 6b). Among the three MTCs, the Ekman component is best correlated with $\frac{\partial D20a}{\partial t}$ in the eastern Pacific (east of 120° W). Since the geostrophic MTC does not contribute to $\frac{\partial D20a}{\partial t}$ in the eastern Pacific (black curve, Fig. 6a), the Ekman component is the main driver in this area.

Overall, an out-of-phase relation between the geostrophic and Ekman components (or the compensating behavior) is present in the whole longitude range, especially in the western and central equatorial Pacific (red curve, Fig. 6b). The equatorial MTCs show systematic longitudinal variations with an out-of-phase tendency between the western-central and the eastern Pacific. That is expected with westerly anomalies in the west and easterly anomalies in the east during El Niño and vice versa during La Niña. The Sverdrup MTC, mostly in phase with the geostrophic MTC, dominates $\frac{\partial D20a}{\partial t}$ in the central and western Pacific. In the eastern equatorial Pacific, the Ekman MTC seems the sole contributor to $\frac{\partial D20a}{\partial t}$.

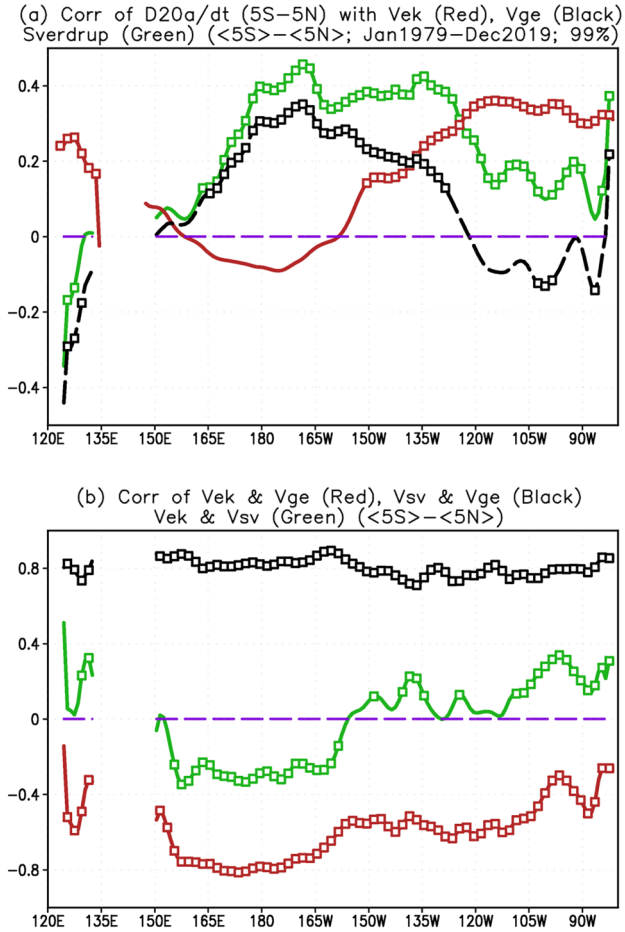

Fig. 6 Longitudinal evolution of the correlations of **a** $\frac{\partial D20a}{\partial t}$ averaged 5° S–5° N with the Ekman (red), geostrophic (black), and Sverdrup (green) MTCs between 5° S and 5° N, and **b** the Ekman MTC with the geostrophic MTC (red), the Ekman MTC with the Sverdrup MTC (green), and the Sverdrup MTC with the geostrophic MTC (black) between 5° S and 5° N. The curve segments with open squares represent the significance at the level of 1% using a t-test. The dashed line represents zero line

5 Connection with the ENSO cycle

Previous studies have shown that the MTCs are linked with the WWV variations and the phase transition of an ENSO cycle (e.g., Meinen and McPhaden 2000, 2001; Izumo 2005; Bosc and Delcroix 2008, and references therein). For instance, Bosc and Delcroix (2008) noted that anomalous meridional geostrophic transports of warm water are out-of-phase with and proportional to the SSTAs in the Niño3.4 region. The correlations of $\frac{dWWV}{dt}$ with (a) the Niño3.4 index, zonally (120° E–80° W) averaged (b) geostrophic, (c) Ekman, and (d) Sverdrup MTCs between 5° S and 5° N are shown in Fig. 7. The maximum negative correlation is present when the Niño3.4 index leads $\frac{dWWV}{dt}$ by 1 month (Fig. 7a). This suggests that, slightly after the peaking of an El Niño (a La Niña), the WWV in the equatorial Pacific is being discharged (recharged) most rapidly. This discharge/recharge of the WWV is conducted through the basin-wide MTC as the maximum positive correlation occurs when the Sverdrup MTC leads $\frac{dWWV}{dt}$ by 0 months (Fig. 7c). Between the two components of the Sverdrup MTC, the maximum positive correlation is present when the geostrophic MTC leads $\frac{dWWV}{dt}$ by 2 months (Fig. 7b), and the maximum negative correlation occurs when the Ekman component leads $\frac{dWWV}{dt}$ by 3 months (Fig. 7c).

This relationship between $\frac{dWWV}{dt}$ and the MTCs is consistent with the more conventional statistics used to measure the WWV-ENSO connection. Figure 8 shows the lead–lag correlations of the Niño3.4 index with (a) the WWV index, zonally (120° E–80° W) averaged (b) geostrophic, (c) Ekman, and (d) Sverdrup MTCs between 5° S and 5° N. The maximum positive correlations between the Niño3.4 and WWV indices are present when the WWV index leads the Niño3.4 index by 4–8 months (Fig. 8a), consistent with that WWV is a crucial precursor of ENSO evolution and forecast (Meinen and McPhaden 2000; Tseng et al. 2016; Hu et al. 2017a; Clarke and Zhang 2019; Zhao et al. 2021). The correlation of the Niño3.4 index with the geostrophic MTC is negative and reaches the maximum absolute value when the Niño3.4 index lags the geostrophic MTC by 1 month (Fig. 8b). In contrast, the correlation of the Niño3.4 index with the Ekman component is positive and reaches the maximum when the Niño3.4 index lags the Ekman component by 2–3 months (Fig. 8c).

Both the zonally uniform and non-uniform components of the MTCs contribute to the ENSO evolution. Here we focus on the roles of the MTCs not only on the WWV and the phase transition of the ENSO cycle but also on the east–west difference of the heat content variation, as well as their lead–lag relations with the ENSO evolution. For this purpose, we conduct a composite analysis with respect to evolving phases of ENSO. Similar to Hu et al. (2019), the ENSO cycle is divided into 14 phases with a 0.5 °C interval based on the observed Niño3.4 index and its tendency (Table 2). Then the composites are made based on the 14 phases of the ENSO cycle (Figs. 9, 10). Following the discharge/recharge paradigm, we examine the WWV (zonally uniform; Fig. 9) and tilt (zonally non-uniform; Fig. 10) modes separately.

It is shown that $\frac{dWWV}{dt}$ (Fig. 9b) is nearly out of phase with SSTA. In particular, the peaks of $\frac{dWWV}{dt}$ are roughly simultaneous with those of SSTA, i.e., the peaking ENSO phases are also the time of fastest WWV decline. However, the decay of $\frac{dWWV}{dt}$ is slower than that of SSTA. As a result, $\frac{dWWV}{dt} = 0$ presents with the WWV at maximum (minimum) in the growing phase of El Niño (La Niña), consistent with the discharge/recharge theory (Jin 1997a, b). Interestingly, the amplitude of the negative $\frac{dWWV}{dt}$ is larger than that of the positive one (Fig. 10b), consistent with the asymmetry of the

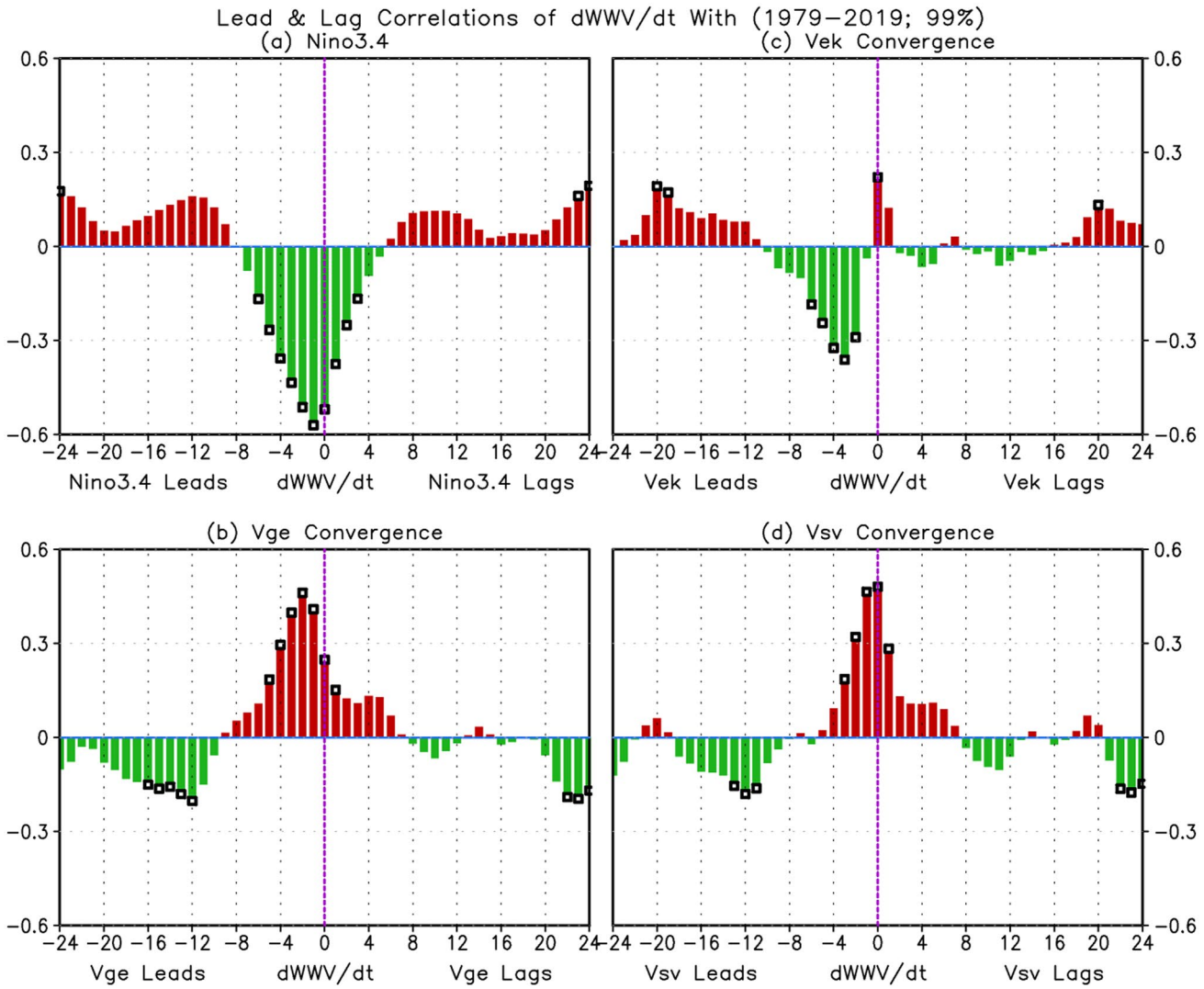

Fig. 7 Lead–lag correlations of $\frac{dWWV}{dt}$ with **a** the Niño3.4 index, 120° E–80° W zonally averaged **b** geostrophic, **c** Ekman, and **d** Sverdrup MTCs between 5° S and 5° N. The bars with open squares represent the significance at the level of 1% using a t-test with independent sample sizes which are estimated following Bretherton et al. (1999)

recharge and discharge processes (Meinen and McPhaden 2000; Hu et al. 2017b). The discharge associated with El Niño is stronger than the recharge associated with La Niña (Kessler 2002; Hu et al. 2017b; Clarke and Zhang 2019). During the ENSO peak phase, the Sverdrup MTC (Fig. 9c) is a major driver of $\frac{dWWV}{dt}$. The evolution of the Sverdrup MTC is more similar to that of the SSTA than $\frac{dWWV}{dt}$. The geostrophic MTC (Fig. 9d) is in phase with the Sverdrup MTC (Fig. 9c) and has larger amplitudes. The Ekman MTC (Fig. 9e) is generally out-of-phase with Sverdrup MTC and has smaller amplitudes. Interestingly, the Ekman MTC is more substantial during the ENSO growth and peak phases but negligible during the decaying phases.

Then we remove the zonal means (i.e., the WWV mode) to examine the MTCs' contributions to the tilt mode (Clarke 2010; Kumar and Hu 2014). Figure 10a shows the zonally varying part of the SSTA, which is dominated by opposite anomalies in the western and eastern Pacific in the ENSO peak phases. The zonal-mean departure SSTA (Fig. 10a) is a noticeable asymmetry between El Niño and La Niña, with the former having a stronger anomalous tilt. In comparison, $\frac{\partial D20a}{\partial t}$ (Fig. 10c) is more symmetric between the warm and cold ENSO episodes. In general, the D20 level is shoaling (deepening) east (west) of 150° W from the peak of El Niño to the peak of La Niña. $\frac{\partial D20a}{\partial t}$ is largely in phase with the zonal mean of the time tendency of the surface zonal wind anomalies (Fig. 10b), consistent with the equatorial Sverdrup balance. Interestingly, climatologically, westward propagation is dominated in $\frac{\partial D20}{\partial t}$, total MTC, and Sverdrup MTC (Fig. 1a–c), while the anomalous evolution of $\frac{\partial D20a}{\partial t}$ and

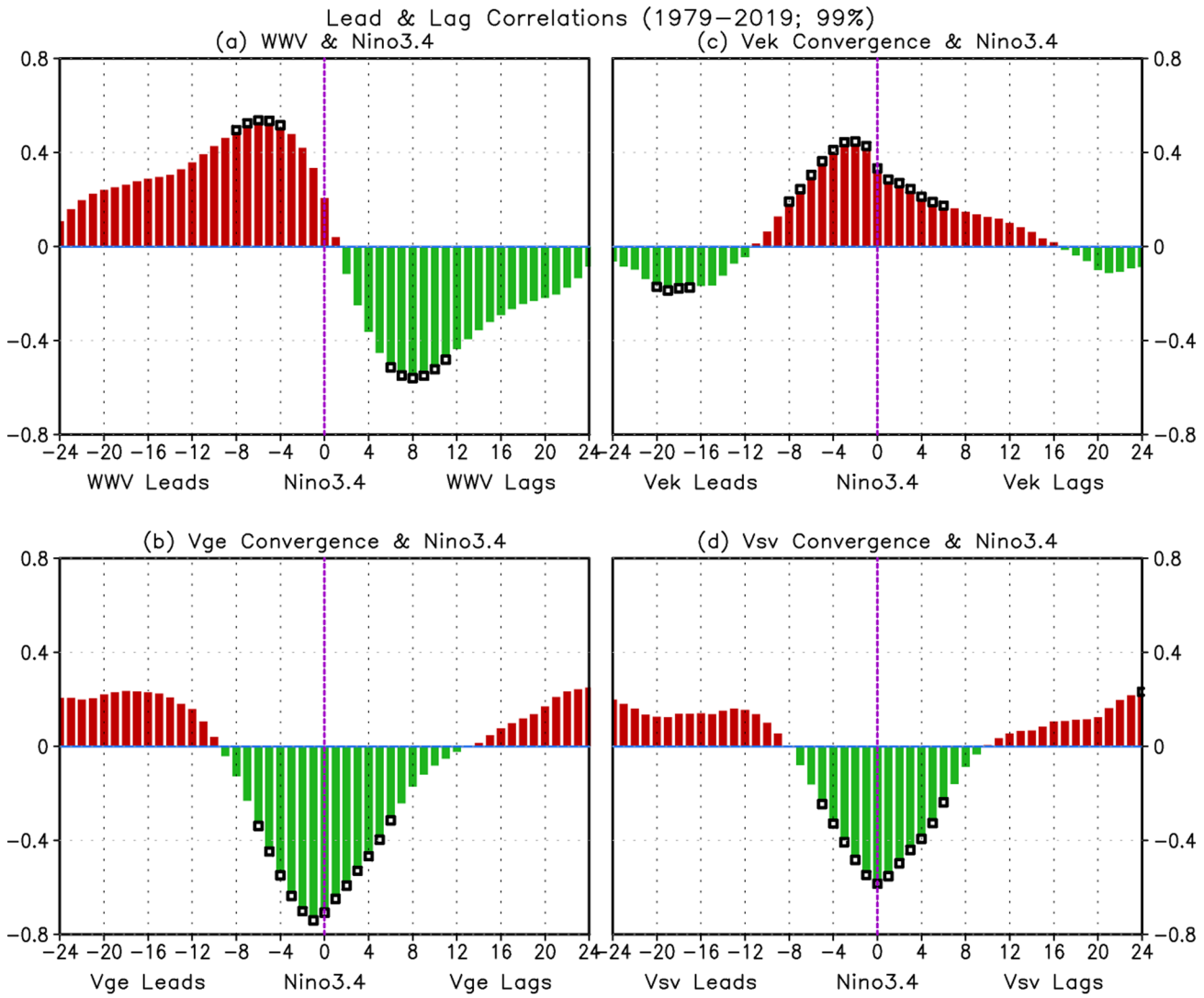

Fig. 8 Lead–lag correlations of the Niño3.4 index with **a** the WWV index, 120° E–80° W zonally averaged **b** geostrophic, **c** Ekman, and **d** Sverdrup MTCs between 5° S and 5° N. The bars with open squares represent the significance at the level of 1% using a t-test with independent sample sizes which are estimated following Bretherton et al. (1999)

Sverdrup MTC associated with the ENSO cycle (Fig. 10c, d) is largely a stationary variation. In addition to the contribution of the MTC, the zonal transport may be important for the dipole-like oscillation of the thermocline (tilt mode).

The zonally varying part of the geostrophic MTC (Fig. 10f) shows convergence (divergence) east (west) of 150° W during El Niño. This pattern favors positive (negative) $\frac{\partial D20a}{\partial t}$ in the east (west), which enhances and prolongs the flattened thermocline during El Niño. Similarly, the geostrophic MTC enhances and prolongs the steeper thermocline during La Niña. The Ekman MTC (Fig. 10e) is generally opposite to that of the geostrophic MTC. As a result, the Sverdrup MTC (Fig. 10d) shows a similar pattern as that of the geostrophic MTC but with a smaller magnitude. Thus, the zonally varying MTC affects the tilt mode.

Accompanied with the growth of an El Niño (La Niña) (Fig. 10a), a dipole-like pattern of $\frac{\partial D20a}{\partial t}$ (Fig. 10c) emerges, which is associated with the so-called anomalous tilt (or dipole) mode (Meinen and McPhaden 2000; Clarke 2010), reflecting the opposite variation of the thermocline between the central and eastern equatorial Pacific (Kumar and Hu 2014). The MTC terms are confined to the central Pacific with a small fraction of the eastward propagation (Fig. 10d–f), in particular for the Ekman component (Fig. 10e). Specifically, the evolution of the Sverdrup and geostrophic MTCs (Fig. 10d, f) are largely in phase with that of the $\frac{\partial D20a}{\partial t}$ (Fig. 10c) and the evolution of the Ekman component (Fig. 10e) is out-of-phase with that of $\frac{\partial D20a}{\partial t}$ (Fig. 10c). This implies that the geostrophic (and Sverdrup) MTCs facilitate the phase transition of the ENSO cycle, and

Table 2 ENSO phase classification based on observed Niño3.4 SSTA range and its tendency during January 1979–December 2019

Phase	SSTA range	SSTA tendency	% of each phase
1	0.0 to 0.5 °C	Positive	13
2	0.5 to 1.0 °C	Positive	7
3	1.0 to 1.5 °C	Positive	3
4	> 1.5 °C	Both positive and negative	6
5	1.5 to 1.0 °C	Negative	3
6	1.0 to 0.5 °C	Negative	7
7	0.5 to 0.0 °C	Negative	9
8	0.0 to -0.5 °C	Negative	13
9	− 0.5 to − 1.0 °C	Negative	7
10	− 1.0 to − 1.5 °C	Negative	3
11	< − 1.5 °C	Both positive and negative	4
12	− 1.5 to − 1.0 °C	Positive	4
13	− 1.0 to − 0.5 °C	Positive	9
14	− 0.5 to 0.0 °C	Positive	12

The numbers in the rightmost column show the % of the number of months in each phase to total months in all phases

the Ekman MTC compensatively hinders the phase transition. Such a feature is also evident in the corresponding zonal-mean anomalies (Fig. 9).

These results indicate that variations of both the geostrophic and Ekman components slightly lead the variations of the Niño3.4 index, but the former has a negative contribution, and the latter has a positive contribution. Therefore, the divergence of warm water from the equatorial Pacific by the geostrophic current helps to terminate the growth of the warm SSTA, favoring the phase transition of ENSO, while the convergence by the Ekman flow prolongs it, not favoring the phase transition of ENSO.

6 Summary and discussion

In this work, using reanalysis data, we investigate the connection of MTC along the equatorial Pacific with the variation of WWV in the equatorial Pacific that is associated with the recharge and discharge processes and the ENSO evolution. The different characteristics of the Sverdrup, geostrophic, and Ekman MTCs along the equatorial Pacific

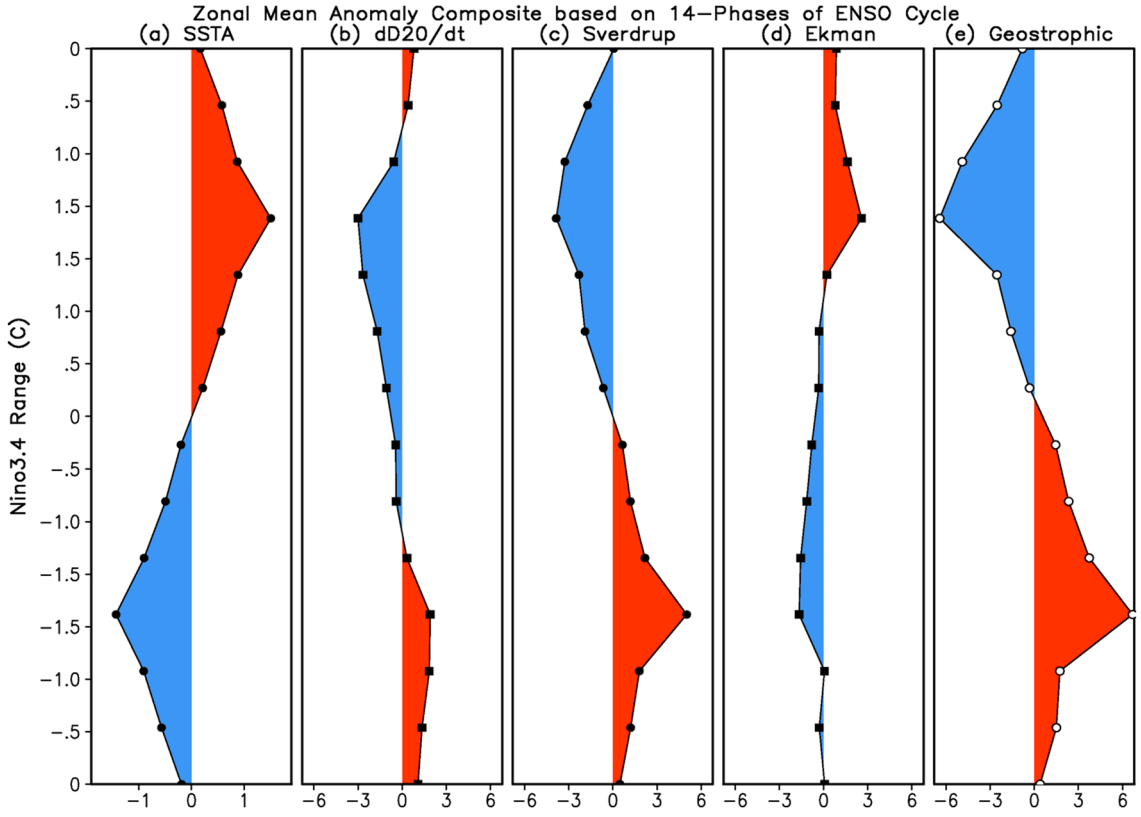

Fig. 9 Zonal-mean (120° E–80° W) composites of **a** SSTA, **b** $\frac{\partial D20a}{\partial t}$ averaged in 5° S–5° N, and **c** Sverdrup, **d** Ekman, and **e** geostrophic MTCs between 5° S and 5° N varied with the 14 phases of the ENSO cycle (y-axis). The 14 phases of the ENSO cycle are determined by the observed Niño3.4 index value and its tendency (see Table 2). The units are C in **a** and m/month in **b–e**

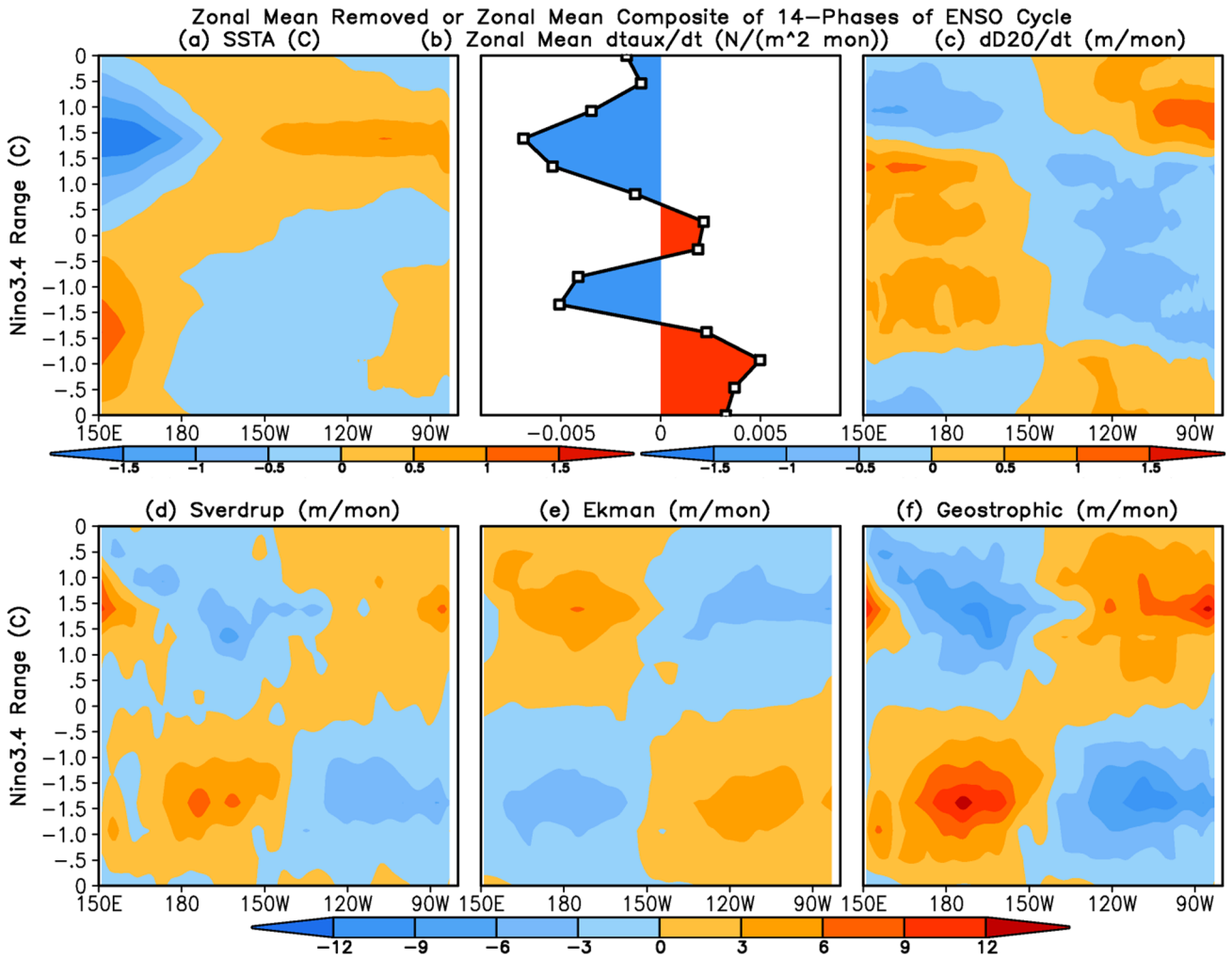

Fig. 10 Zonal-mean departure anomaly composites of **a** SST and **c** $\frac{\partial D20}{\partial t}$ averaged in 5° S–5° N, **d** Sverdrup, **e** Ekman, and **f** geostrophic MTCs between 5° S and 5° N varied with the longitude (x-axis) and 14 phases of the ENSO cycle (y-axis), and **b** zonal mean of time tendency of zonal wind stress anomalies varied with the 14 phases of the ENSO cycle (y-axis). The 14 phases of the ENSO cycle are determined by the observed Niño3.4 index value and its tendency (see Table 2). The units are C in **a**, N/(m^2 month) in **b**, and m/month in **c**–**f**

are examined, focusing on their longitudinal variations in connecting with the WWV variation and ENSO evolution.

Statistically, the amplitudes of variations are largest for the geostrophic component and smallest for the Ekman component, and in between for the Sverdrup MTC. Spatially, the maximum variabilities appear in the central Pacific around 160° E–165° W for both the geostrophic and Sverdrup MTCs. The Sverdrup MTC is largely determined by the geostrophic component. There is compensation between the geostrophic and Ekman components which is mainly in the central Pacific. For the contribution to the thermocline fluctuation along the equatorial Pacific, the Ekman component has a significant contribution in 150° W eastward to the coast as well as the far-western Pacific, while the geostrophic component has a significant contribution in the central and east-central Pacific (165° E–135° W) with some significant contributions in the far-western and eastern Pacific. The Sverdrup MTC has a significant contribution in almost the entire equatorial Pacific, except in the far-western and far-eastern Pacific near the coasts.

For the entire equatorial Pacific average, both the geostrophic and Ekman components slightly lead the variations of the Niño3.4 index, with the former having a positive correlation and the latter having a negative correlation. In the El Niño (La Niña) phase, weakened (strengthened) trade wind along the equatorial Pacific leads to positive (negative) Ekman MTC anomaly, not favoring the phase transition from El Niño to La Niña (from La Niña to El Niño); meanwhile, the corresponding positive (negative) wind stress curl anomaly in the tropical Northern Hemisphere and negative

(positive) wind stress curl anomaly in the tropical Southern Hemisphere result in negative (positive) geostrophic MTC anomaly along the equator, favoring the phase transition (Fig. 11). Thus, the geostrophic (and Sverdrup) MTCs facilitate the phase transition of the ENSO cycle, while the Ekman MTC compensatively hinders the phase transition. The longitudinally varying component of the MTC may also enhance the tilt mode during the ENSO growth and maturing phases. As a result of the compensation and dominance of the geostrophic component in the Sverdrup MTC, the amplitude of the maximum negative correlation between the Niño3.4 index and the geostrophic component is larger than that between the Niño3.4 index and the Sverdrup MTC. Here, we focused on the contribution of MTC to the thermocline tilt oscillation. It should be pointed out that the zonal transport may also play an important role in modulating the opposite variation of the thermocline between the western and eastern equatorial Pacific (tilt mode).

These results showed the different contributions of the geostrophic and Ekman MTCs to the thermocline fluctuation along the equatorial Pacific and identified the crucial longitude zones of the different components of the MTCs in linking to the WWV and ENSO evolutions. This may benefit the understanding, monitoring, and forecasting ENSO that is a leading source of global climate variability and predictability at the seasonal-interannual time scales. For example, surface wind stress-induced Ekman MTC is mainly in the eastern equatorial Pacific, while surface wind stress curl-induced geostrophic MTC is mainly in the central and east-central Pacific.

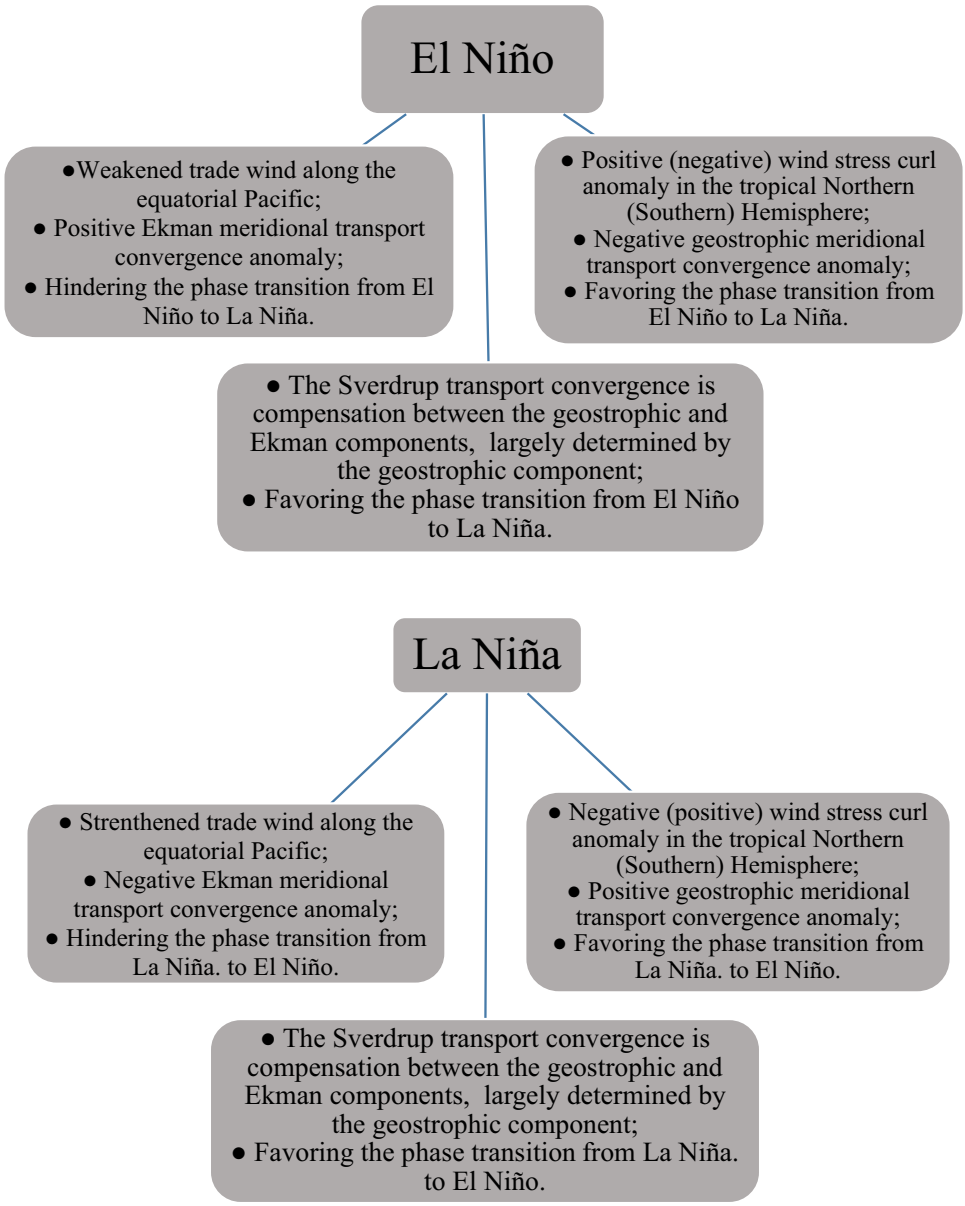

Fig. 11 Schematic plot to show the connections of wind stress anomaly, the Sverdrup, geostrophic, and Ekman meridional transport convergence anomalies with the ENSO phase transition in El Niño (top) and La Niña (bottom) conditions

The focus of this study is on the meridional mass transports in the tropics at interseasonal–interannual time scales and their association with ENSO evolution. In particular, the Sverdrup transport is associated with the oceanic anomalies generated by the surface wind stress curls in the interior of the basin. Furthermore, the meridional transports at 5° S and 5° N are still within the equatorial waveguide (e.g., Battisti 1989). However, large oceanic anomalies are also present in the higher latitudes (such as 12° N), which contribute to the lower frequency components of ENSO (Kirtman 1997). Kirtman (1997) further pointed out that the oceanic anomalies outside the equatorial waveguide (i.e., poleward of around 7° of latitudes) influence ENSO mainly through the westward propagating off-equatorial Rossby waves to the western boundary. These transports associated with the oceanic wave dynamics are not counted for in this study. The roles of the tropical and subtropical oceanic anomalies in the ENSO cycle and its interdecadal variations have been demonstrated by previous studies (Graham and White 1988, 1991; Battisti 1989; White et al. 1989; Kessler 1990; McCreary and Lu 1994; Zhang and Levitus 1996; Gu and Philander 1997; Zhang et al. 1998; Barnett et al. 1999; Kleeman et al. 1999; Liu et al. 2002). For example, oceanic thermal anomalies can coherently propagate along the loop consisting of the off-equatorial region along 12° N, the western boundary, the equator, and the eastern boundary (Zhang and Levitus 1996; Zhang et al. 1998). Thus, the possible connection of the anomalies in the tropical region and higher latitude atmosphere–ocean anomalies deserves further investigation.

Finally, our study concentrates on the roles played by the MTCs. One should note that the ocean wave dynamics also play an important role in influencing both the WWV and tilt modes during an ENSO cycle. Some recent studies have argued that WWV plays a key dynamical role in ENSO which may not be because of heat content, but mainly because it is a proxy for zonally-averaged zonal equatorial currents. For example, Clarke and Zhang (2019) suggested that WWV can be an ENSO predictor mainly because it is directly related to the anomalous equatorial zonal current and its acceleration. These anomalous zonal equatorial currents advect the eastern edge of the western equatorial Pacific warm pool eastward during the development stage of the El Niño and the cold water in the eastern equatorial Pacific westward during that of La Niña (Picaut et al. 1997). When the equatorial westerly wind anomalies move south of the equator during the boreal winter of an El Niño event (Harrison and Vecchi 1999; Stuecker et al. 2013) and the zonal equatorial wind anomalies are weakened on the equator, the sea level and thermocline anomalies decrease in the eastern equatorial Pacific. Chen et al. (2016) also argued that the shoaling of the equatorial thermocline, together with a simultaneous deepening of the off-equatorial thermocline, triggers a sudden basin-wide reversal of anomalous equatorial zonal transport above the thermocline at the peaking phase of ENSO that rapidly terminates an El Niño event. Zhang and Clarke (2017) and Clarke and Zhang (2019) further argued that this adjustment of the equatorial Pacific is closely related to the reduction of the equatorial WWV. These results have further demonstrated the complexity of the atmosphere–ocean interactions and their roles in ENSO evolution.

Acknowledgements The authors thank the reviewers for their constructive comments and insightful suggestions. GODAS and surface wind stress data from the National Environmental Prediction Center and Department of Energy reanalysis are available through Behringer (2007) and Li et al. (2020), and Kanamitsu et al. (2002), respectively. The data used in this study can be downloaded from https://www.esrl.noaa.gov/psd/data/gridded/data.godas.html and https://psl.noaa.gov/data/gridded/data.ncep.reanalysis2.html, or contact us via xiaofanli@zju.edu.cn. X. L. is supported by the National Natural Science Foundation of China (41930967). Z. H. is supported by the NOAA CTB project NA20OAR4590316. B. H. is supported by the NOAA MAPP drought project (NA17OAR4310144).

References

Barnett TP, Pierce DW, Latif M, Dommenget D, Saravanan R (1999) Interdecadal interactions between the tropics and mid-latitudes in the Pacific basin. Geophys Res Lett 26:615–618

Battisti DS (1989) On the role of off-equatorial oceanic Rossby waves during ENSO. J Phys Oceanogr 19(4):551–559

Behringer DW (2007) The Global Ocean Data Assimilation System (GODAS) at NCEP. Preprints, 11th Symposium on Integrated Observing and Assimilation Systems for Atmosphere, Oceans, and Land Surface, San Antonio, TX, Amer Meteor Soc 3.3. http://ams.confex.com/ams/87ANNUAL/techprogram/paper_119541.htm. Accessed 16 Jan 2007

Bjerknes J (1969) Atmospheric teleconnections from the equatorial Pacific. Mon Weather Rev 97:163–172

Bosc C, Delcroix T (2008) Observed equatorial Rossby waves and ENSO-related warm water volume changes in the equatorial Pacific Ocean. J Geophys Res Oceans 113:C06003. https://doi.org/10.1029/2007JC004613

Bretherton CS, Widmann M, Dymnikov VP, Wallace JM, Blade I (1999) Effective number of degrees of freedom of a time-varying field. J Clim 12:1990–2009. https://doi.org/10.1175/1520-0442(1999)012%3c1990:TENOSD%3e2.0.CO;2

Brown JN, Fedorov AV (2010) Estimating the diapycnal transport contribution to warm water volume variations in the tropical Pacific Ocean. J Clim 23(2):221–237. https://doi.org/10.1175/2009JCLI2347.1

Cane MA, Sarachik ES (1981) The periodic response of a linear baroclinic equatorial ocean. J Mar Res 39:651–693

Chen H-C, Hu Z-Z, Huang B, Sui C-H (2016) The role of reversed equatorial zonal transport in terminating an ENSO event. J Clim 29(16):5859–5877. https://doi.org/10.1175/JCLI-D-16-0047.1

Chen H-c, Tseng Y-h, Hu Z-Z, Ding R (2020) Enhancing the ENSO predictability beyond the spring barrier. Sci Rep 10:984. https://doi.org/10.1038/s41598-020-57853-7

Clarke AJ (2010) Analytical theory for the quasi-steady and low-frequency equatorial ocean response to wind forcing: the "tilt"

and "warm water volume" modes. J Phys Ocean 40(1):121–137. https://doi.org/10.1175/2009JPO4263.1
Clarke AJ, Van Gorder S (2001) ENSO prediction using an ENSO trigger and a proxy for western equatorial Pacific warm pool movement. Geophys Res Lett 28:579–582. https://doi.org/10.1029/2000GL012201
Clarke AJ, Zhang X (2019) On the physics of the warm water volume and El Niño/La Niña predictability. J Phys Oceanogr 49:1541–1560. https://doi.org/10.1175/JPO-D-18-0144.1
Clarke AJ, Van Gorder S, Colantuono G (2007) Wind stress curl and ENSO discharge/recharge in the equatorial Pacific. J Phys Ocean 37(4):1077–1091. https://doi.org/10.1175/JPO3035.1
Graham NE, White WB (1988) The E1 Niño/Southern Oscillation as a natural oscillator of the tropical Pacific Ocean-atmosphere system. Science 240:1293–1302
Graham NE, White WB (1991) Comments on "On the role of off-equatorial oceanic Rossby waves during ENSO." J Phys Oceanogr 21:453–460
Gu D-F, Philander SGH (1997) Interdecadal climate fluctuations that depend on exchanges between the tropical and extratropics. Science 275:805–807
Harrison DE, Vecchi GA (1999) On the termination of El Niño. Geophys Res Lett 26:1593–1596
Hu Z-Z, Kumar A, Zhu J, Huang B, Tseng Y-h, Wang X (2017a) On the shortening of the lead time of ocean warm water volume to ENSO SST since 2000. Sci Rep 7:4294. https://doi.org/10.1038/s41598-017-04566-z
Hu Z-Z, Kumar A, Huang B, Zhu J, Zhang R-H, Jin F-F (2017b) Asymmetric evolution of El Niño and La Niña: the recharge/discharge processes and role of the off-equatorial sea surface height anomaly. Clim Dyn 49(7–8):2737–2748. https://doi.org/10.1007/s00382-016-3498-4
Hu Z-Z, Kumar A, Zhu J, Peng P, Huang B (2019) On the challenge for ENSO cycle prediction: an example from NCEP Climate Forecast System version 2. J Clim 32(1):183–194. https://doi.org/10.1175/JCLI-D-18-0285.1
Hu Z-Z, Kumar A, Jha B, Huang B (2020a) How much of monthly mean precipitation variability over global land is associated with SST anomalies? Clim Dyn 54(1–2):701–712. https://doi.org/10.1007/s00382-019-05023-5
Hu Z-Z, Kumar A, Huang B, Zhu J, L'Heureux M, McPhaden MJ, Yu J-Y (2020b) The interdecadal shift of ENSO properties in 1999/2000: a review. J Clim 33(11):4441–4462. https://doi.org/10.1175/JCLI-D-19-0316.1
Huang B et al (2017) Reforecasting the ENSO events in the past 57 years (1958–2014). J Clim 30:7669–7693. https://doi.org/10.1175/JCLI-D-16-0642.1
Huang B, Shin C-S, Kumar A (2019) Predictive skill and predictive patterns of the US seasonal precipitation in CFSv2 reforecasts of sixty years (1958–2017). J Clim 32:8603–8637. https://doi.org/10.1175/JCLI-D-19-0230.1
Izumo T (2005) The equatorial undercurrent, meridional overturning circulation, and their roles in mass and heat exchanges during El Niño events in the tropical Pacific Ocean. Ocean Dyn 55:110–123. https://doi.org/10.1007/s10236-005-0115-1
Izumo T, Lengaigne M, Vialard J, Suresh I, Planton Y (2019) On the physical interpretation of the lead relation between Warm Water Volume and the El Niño Southern Oscillation. Clim Dyn 52:2923–2942. https://doi.org/10.1007/s00382-018-4313-1
Jin F-F (1997a) An equatorial ocean recharge paradigm for ENSO. Part I: conceptual model. J Atmos Sci 54:811–829. https://doi.org/10.1175/1520-0469(1997)054%3c0811:AEORPF%3e2.0.CO;2
Jin F-F (1997b) An equatorial ocean recharge paradigm for ENSO. Part II: a stripped-down coupled model. J Atmos Sci 54:830–847. https://doi.org/10.1175/1520-0469(1997)054%3c0830:AEORPF%3e2.0.CO;2
Kanamitsu M et al (2002) NCEP–DOE AMIP–II reanalysis (R–2). Bull Am Meteorol Soc 83:1631–1643. https://doi.org/10.1175/BAMS-83-11-1631
Kessler WS (1990) Observations of long Rossby waves in the northern tropical Pacific. J Geophys Res 95(C4):5183–5217
Kessler WS (2002) Is ENSO a cycle or a series of events? Geophys Res Lett 29(23):2125. https://doi.org/10.1029/2002GL015924
Kirtman BP (1997) Oceanic Rossby wave dynamics and the ENSO period in a coupled model. J Climate 10:1690–1704
Kleeman R, McCreary JP, Klinger BA (1999) A mechanism for generating ENSO decadal variability. Geophys Res Lett 26:1743–1746
Kug J-S, Kang I-S, An S-I (2003) Symmetric and antisymmetric mass exchanges between the equatorial and off-equatorial Pacific associated with ENSO. J Geophys Res 108:3284. https://doi.org/10.1029/2002JC001671
Kug J-S, An S-I, Jin F-F et al (2005) Preconditions for El Niño and La Niña onsets and their relation to the Indian Ocean. Geophys Res Lett 32:L05706. https://doi.org/10.1029/2004GL021674
Kumar A, Hu Z-Z (2014) Interannual and interdecadal variability of ocean temperature along the equatorial Pacific in conjunction with ENSO. Clim Dyn 42(5–6):1243–1258. https://doi.org/10.1007/s00382-013-1721-0
Lengaigne M, Hausmann U, Madec G et al (2021) Mechanisms controlling warm water volume interannual variations in the equatorial Pacific: diabatic versus adiabatic processes. Clim Dyn 38:1031–1046. https://doi.org/10.1007/s00382-011-1051-z
Li X, Hu Z-Z, Huang B, Jin F-F (2020) On the interdecadal variation of the warm water volume in the tropical Pacific around 1999/2000. J Geophys Res Atmos 125(18):e2020JD033306. https://doi.org/10.1029/2020JD033306
Liu Z, Wu L, Gallimore R, Jacob G (2002) Search for the origins of Pacific decadal climate variability. Geophys Res Lett 29:1404. https://doi.org/10.1029/2001GL013735
Lu Q, Ruan Z, Wang D, Chen D, Wu Q (2017) Zonal Transport from the western boundary and its role in warm water volume changes during ENSO. J Phys Oceanogr 47:211–225. https://doi.org/10.1175/JPO-D-16-0112.1
McCreary JP, Lu P (1994) Interaction between the subtropical and equatorial ocean circulations: the subtropical cell. J Phys Oceanogr 24:466–497
McGregor S et al (2014) ENSO-driven interhemispheric Pacific mass transports. J Geophys Res Oceans 119:6221–6237. https://doi.org/10.1002/2014JC010286
McPhaden MJ (2012) A 21st century shift in the relationship between ENSO SST and warm water volume anomalies. Geophys Res Lett 39:L09706. https://doi.org/10.1029/2012GL051826
McPhaden MJ, Taft BA (1988) On the dynamics of seasonal and intraseasonal variability in the eastern equatorial Pacific. J Phys Oceanogr 18:1713–1732
McPhaden MJ, Zhang X, Hendon HH, Wheeler MC (2006) Large scale dynamics and MJO forcing of ENSO variability. Geophys Res Lett 33:L16702. https://doi.org/10.1029/2006GL026786
Meinen CS, McPhaden MJ (2000) Observations of warm water volume changes in the equatorial Pacific and their relationship to El Niño and La Niña. J Clim 13:3551–3559. https://doi.org/10.1175/1520-0442
Meinen CS, McPhaden MJ (2001) Interannual variability in warm water volume transports in the equatorial Pacific during 1993–99. J Phys Oceanogr 31:1324–1345. https://doi.org/10.1175/1520-0485(2001)031%3c1324:IVIWWV%3e2.0.CO;2
National Research Council (2010) Assessment of intraseasonal to interannual climate prediction and predictability. The National Academies Press, Washington, DC (**ISBN-10: 0-309-15183-X**)
Pedlosky J (1996) Ocean circulation theory. Springer, Heidelberg, p 453

Picaut J, Masia F, du Penhoat Y (1997) An advective-reflective conceptual model for the oscillatory nature of the ENSO. Science 277:663–666

Schneider EK, Huang B, Shukla J (1995) Ocean wave dynamics and El Niño. J Climate 8:2415–2439

Singh A, Delcroix T (2013) Eastern and central Pacific ENSO and their relationships to the recharge/discharge oscillator paradigm. Deep-Sea Res I 82:32–43. https://doi.org/10.1016/j.dsr.2013.08.002

Springer S, McPhaden MJ, Busalacchi AJ (1990) Oceanic heat content variability in the tropical Pacific during the 1982–83 El Niño. J Geophys Res 95:22089–22102

Stuecker MF, Timmermann A, Jin F-F, McGregor S, Ren H-L (2013) A combination mode of the annual cycle and the El Niño/Southern Oscillation. Nat Geosci 6:540–544. https://doi.org/10.1038/ngeo1826

Tseng Y-H, Hu Z-Z, Ding R-Q et al (2016) An ENSO prediction approach based on ocean conditions and ocean–atmosphere coupling. Clim Dyn 48(5–6):2025–2044. https://doi.org/10.1007/s00382-016-3188-2

Wang C (2001) A unified oscillator model for the El Niño-Southern Oscillation. J Clim 14:98–115. https://doi.org/10.1175/1520-0442(2001)014%3c0098:AUOMFT%3e2.0.CO;2

Wang C, Deser C, Yu J-Y, Di Nezio P, Clement A (2016) El Niño-Southern Oscillation (ENSO): a review. In: Glymn P, Manzello D, Enochs I (eds) Coral reefs of the eastern pacific. Springer Science Publisher, New York, pp 85–106

White WB, He Y, Pazan SE (1989) Off-equatorial westward propagating waves in the tropical Pacific during the 1982–83 and 1986–87 ENSO events. J Phys Oceanogr 19:1397–1406

Wyrtki K (1975) El Niño—the dynamic response of the equatorial Pacific Ocean to atmospheric forcing. J Phys Oceanogr 5:572–584. https://doi.org/10.1175/1520-0485(1975)005%3c0572:ENTDRO%3e2.0.CO;2

Wyrtki K (1985) Water displacements in the Pacific and the genesis of El Niño cycles. J Geophys Res 90(C4):7129–7132. https://doi.org/10.1029/JC090iC04p07129

Yu X, McPhaden MJ (1999) Dynamical analysis of seasonal and interannual variability in the equatorial Pacific. J Phys Oceanogr 29:2350–2369

Zebiak S (1989) Ocean heat content variability and ENSO cycles. J Phys Oceanogr 19:475–485. https://doi.org/10.1175/1520-0485(1989)019%3c0475:OHCVAE%3e2.0.CO;2

Zhang X, Clarke AJ (2017) On the dynamical relationship between equatorial Pacific surface currents, zonally averaged equatorial sea level, and El Niño prediction. J Phys Oceanogr 47:323–337. https://doi.org/10.1175/JPO-D-16-0193.1

Zhang R-H, Levitus S (1996) Structure and evolution of interannual variability of the Tropical Pacific upper ocean temperature. J Geophys Res 101:20501–20524

Zhang R-H, Rothstein LM, Busalacchi AJ (1998) Origin of upper-ocean warming and El Niño change on decadal time scales in the Tropical Pacific Ocean. Nature 391:879–883

Zhang W, Li S, Jin F-F, Xie R, Liu C, Stuecker MF, Xue A (2019) ENSO regime changes responsible for decadal phase relationship variations between ENSO sea surface temperature and warm water volume. Geophys Res Lett. https://doi.org/10.1029/2019GL082943

Zhao S, Jin F-F, Stuecker M (2021) Understanding lead times of warm-water-volumes to ENSO sea surface temperature anomalies. Geophys Res Lett. https://doi.org/10.1029/2021GL094366